PCCP

PAPER

Check for updates

Cite this: *Phys. Chem. Chem. Phys.*, 2018, **20**, 19546

Amorphous graphene: a constituent part of low density amorphous carbon†

Bishal Bhattarai,[a] Parthapratim Biswas,[b] Raymond Atta-Fynn[c] and D. A. Drabold *[d]

Received 21st April 2018,
Accepted 5th July 2018

DOI: 10.1039/c8cp02545b

rsc.li/pccp

In this paper, we provide evidence that low density nano-porous amorphous carbon (a-C) consists of interconnected regions of amorphous graphene (a-G). We include experimental information in producing models, while retaining the power and accuracy of *ab initio* methods with no biasing assumptions. Our models are highly disordered with predominant sp^2 bonding and ring connectivity mainly of sizes 5–8. The structural, dynamical and electronic signatures of our 3-D amorphous graphene are similar to those of monolayer amorphous graphene. We predict an extended x-ray absorption fine structure (EXAFS) signature of amorphous graphene. Electronic density of states calculations for 3-D amorphous graphene reveal similarity to monolayer amorphous graphene and the system is non conducting.

1 Introduction

Amorphous graphene (a-G), an idealized 2-D structure consisting of 5-6-7 polygons with predominant sp^2 bonding, has presented a challenge for extraction. This has been achieved by exposure of an electron beam to a crystalline/pristine graphene (p-graphene) sheet, to produce an amorphous monolayer.[1] Similarly, a-G has been modeled by introducing 5 and 7 membered rings with a *Wooten-Weaire-Winer* (WWW) scheme.[2–5]

The advancement and understanding of amorphous materials has been limited by conventional simulations.[6] A generic approach, "*melt quenching*" (MQ) *via* molecular dynamics (MD), is limited by its quenching rate, and model size (for *ab initio* interactions). Meanwhile, the MQ models prepared using inter-atomic potentials directly depend upon the choice of inter-atomic interactions. A recent work of Li *et al.* has highlighted this by comparing models of amorphous carbon prepared using Tersoff, REBO, and ReaxFF potentials. Alternatively, tight-binding molecular-dynamics (TBMD)[7] and its hybrid modifications[8] are also used as an efficient alternative to model amorphous solids. In contrast, high-precision experimental data from diffraction, infrared (IR), and nuclear magnetic resonance (NMR) are readily available. The reverse Monte Carlo (RMC) method is used to determine the structure of complex materials by inverting experimental diffraction data. This method often leads to unsatisfactory and unphysical results, as scattering data lack sufficient information to uniquely resolve local structural features. This difficulty in the inversion of experimental data has led to several attempts with multiple experimental constraints, which is a difficult optimization problem, and use of hybrid schemes of RMC.[9–12] Hybrid methods incorporate an additional penalty function based on the force fields to the conventional structural refinement of the RMC method. Several variations and implementation of these hybrid approaches have been discussed elsewhere. In this work, we have used a recently developed hybrid approach, namely the FEAR (force enhanced atomic refinement) method, an *ab initio* structural refinement technique, to provide clear evidence that low density phases of carbide-derived carbon (CDC)[13–16] are a form of three dimensional a-G (warped, wrapped 2D a-G sheets with ring disorder and defects).

FEAR is a means to invert diffraction data and simultaneously determine coordinates at a suitable *ab initio* energy minimum, starting from a random configuration. FEAR is an efficient and robust method to model different amorphous systems. It has been so far successfully applied to a-Si, a-SiO_2, Ag-doped $GeSe_3$ and a-C at various densities.[17–20] In the case of amorphous silicon, FEAR has been successfully implemented for up to 1024 atoms.[21]

2 Methodology and models

To tersely recapitulate FEAR, we begin with some definitions. If $V(X_i \ldots X_n)$ is the energy functional for atomic coordinates $\{X_i\}$

[a] *Department of Physics and Astronomy, Condensed Matter and Surface Science Program (CMSS), Ohio University, Athens, Ohio 45701, USA*
[b] *Department of Physics and Astronomy, The University of Southern Mississippi, Hattiesburg, Mississippi 39406, USA*
[c] *Department of Physics, University of Texas, Arlington, Texas 76019, USA*
[d] *Department of Physics and Astronomy, Nanoscale and Quantum Phenomena Institute (NQPI), Ohio University, Athens, Ohio 45701, USA. E-mail: drabold@ohio.edu*

† Electronic supplementary information (ESI) available: Computational details of FEAR and comparison. See DOI: 10.1039/c8cp02545b

 This journal is © the Owner Societies 2018

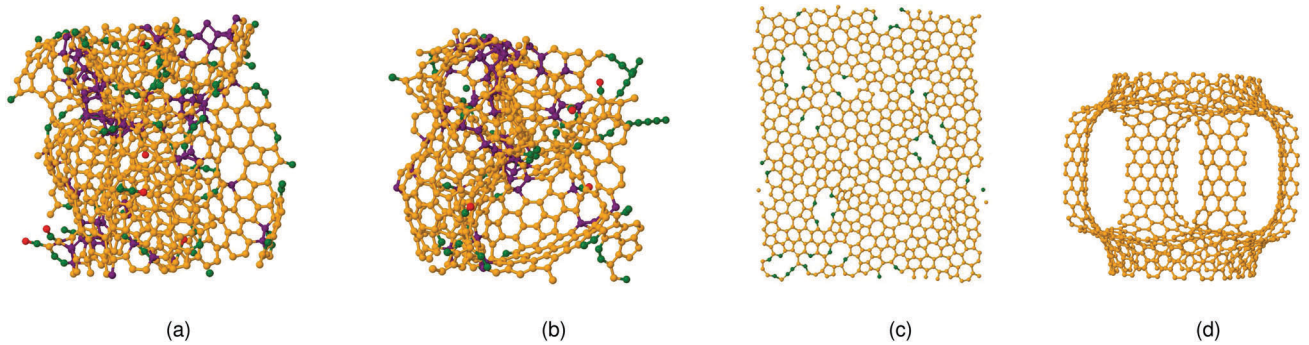

Fig. 1 Structure models: (a) 3-D a-graphene (800 atom), (b) 3-D a-graphene (648 atom), (c) 2-D a-graphene,[4] and (d) 3-D schwarzite.[22] Color coding: purple (sp^3), orange (sp^2), green (sp) and red (singly bonded).

and χ^2 measures the discrepancy between (say) a diffraction experiment and a computer model, we seek to find a set of atomic coordinates $\{X_i\}$ with the property that V = minimum and χ^2 is within the experimental error. FEAR consists of (i) producing a random structural model at an assumed density, (ii) invoking N accepted moves with the Reverse Monte Carlo (RMC) method followed by M conjugate-gradient (CG) relaxation steps using *ab initio* interactions. We then iterate (ii) to convergence (fitting the experimental data and finding a suitable minimum of DFT interactions). Accurate and unbiased chemical information is included in the CG step.

In this paper, a random starting configuration is employed along with the code RMCProfile[24] with values of M = 1 and $N \sim 100$, respectively. We have used silicon carbide-derived nanoporous carbon (SIC-CDC)[23] at a density of 0.95 g cm^{-3} as our experimental data. We have used a maximum RMC step size of 0.15–0.375 Å, restricting the minimum approach distance between atoms to 1.05 Å, a fixed spacing of 0.02 Å and 0.04 weight of the experimental data. The relaxation step was performed with single-ζ basis, periodic boundary conditions and Harris functional at a constant volume using the DFT code SIESTA.[25] Finally, we relax the converged models using the Vienna *ab initio* package (VASP).[26–30] All the calculations were performed with a single k-point $\Gamma(\vec{k} = 0)$ and the local density approximation, and PAW potentials. We started with random initial configurations, and made FEAR models with 216, 648 and 800 atoms. We observe in passing that FEAR is computationally highly advantageous compared to MQ, requiring far fewer calls to the *ab initio* code (in the FEAR CG step). We explore reproducibility with models containing 216, 648 and 800 atoms, and show that a consistent network topology emerges.

To explain and interpret the results, we have created MQ models with 648 and 216 atoms. The 648-atom MQ model was equilibrated at 7000 K, then cooled to 300 K, and after further equilibration at 300 K, was relaxed using the CG method. This process required 50 ps of total simulation time. Due to the large size of the system we have used the DFT code SIESTA with the Harris functional to form this model. We have also created a 216-atom MQ model with the help of the plane wave DFT code VASP, using the local-density approximation with the Ceperley–Alder (CA) exchange correlation functional. The VASP model was first equilibrated at 7500 K and then quenched to 300 K in multiple steps over a total simulation time of 42 ps using a time step of 2 fs. A plane wave cut off of 350 eV and energy difference criteria of 10^{-4} was chosen for the simulation. These are typical simulation times used in preparing accurate models of amorphous systems.‡ In addition, we discuss crystalline/pristine graphene (p-graphene, 800 atoms)[4] and a schwarzite model (792 atoms)[22] for comparison. The details are summarized in Table S1, ESI†.

3 Results and discussion

In Fig. 1, we show the topology of our models. sp^2 bonding (in orange) dominates each of these structures. 3-D amorphous graphene has a few sp^3 bonded sites ($\sim$11%) which mainly connect one sp^2 graphene fragment to another. Similarly, a few sp bonded sites appear in both 3-D and 2-D amorphous graphene. In Fig. 2 (left panel), we compare our results with the experimental results of nano-porous silicon carbide derived carbon (SiC-CDC) at a density of 0.95 g cm^{-3}.[23] We observe good agreement with the experiment (by construction), while a slight deviation is observed upon complete *ab initio* (VASP) relaxation. We have plotted the radial distribution function $g(r)$ for the four models and the static structure factor $S(Q)$ in Fig. 2 (right panel). The 3-D a-graphene model has the first nearest-neighbor distance at 1.42 Å and the second nearest-neighbor distance at 2.45 Å, the same as the crystalline graphene model. Meanwhile, the 2-D a-graphene model[3,4] reveals a second peak in $g(r)$ with the second nearest-neighbor at 2.38 Å, suggesting a broader distribution of bond-angles than the 3-D a-graphene model[7] (see Fig. 3 (right panel)).

‡ It is worth noting that the melt-quench (MQ) process depends on cooling rate. However, our earlier study done for several models of amorphous carbon at different cooling rates showed only slight differences in bonding (sp, sp^2 and sp^3) preferences without much change in other observables such as electronic density of states or vibrational properties.[31] Recently it has been shown that very slow quenching rate improves the quality of MQ models.[32,33] These simulations are very extended and do not seem to be an efficient way to model amorphous systems. FEAR produces models with DFT accuracy taking less CPU time. Computationally speaking, our 216 atom FEAR model presented here requires 1/14 the time used for the 216 atom VASP (MQ) model (Table S1, ESI†) and requires total force calls of ($\sim$6000–8000) to obtain a converged model.

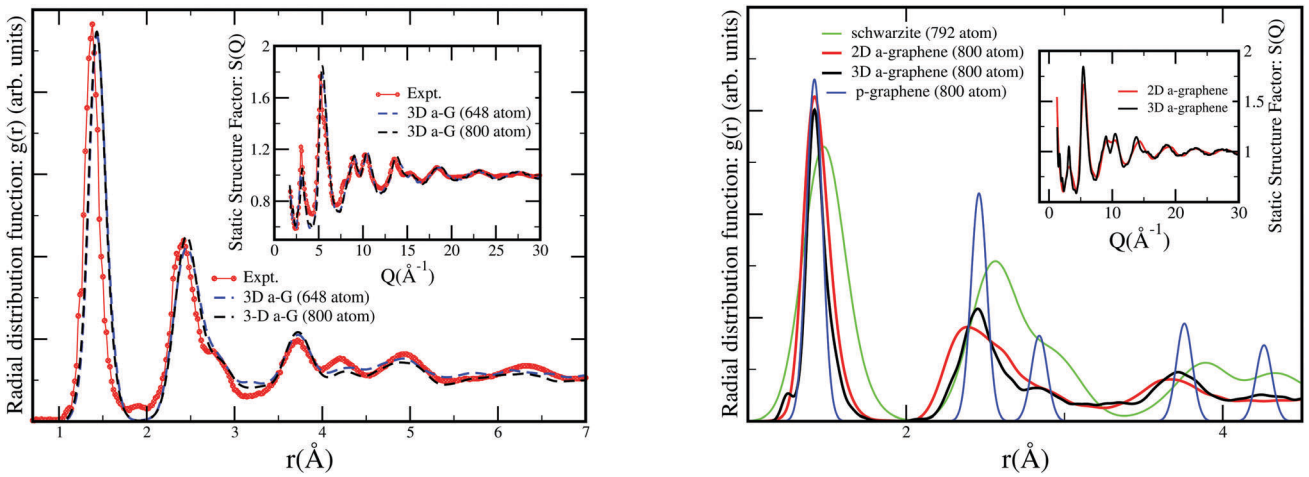

Fig. 2 (Left panel) Comparison of the radial distribution function $g(r)$ and structure factor ($S(Q)$, inset) of the FEAR models with experiments (ρ = 0.95 g cm^{-3}).[23] (Right panel) Radial distribution functions $g(r)$ of four models (3-D a-graphene (800 atom), 2-D a-graphene (800 atom), crystalline/pristine graphene (p-graphene, 800 atom) and schwarzite (792 atom)); (inset) comparison of the static structure factor $S(Q)$ between 3-D and 2-D a-graphene.

Both 2-D and 3-D a-graphene exhibit a bond angle distribution (BAD) with a peak at around ∼120°. The full width at half maximum of the BAD has a value of 27.45° and 26.65° for 2-D and 3-D graphene, respectively. It is observed that with high sp^2 concentration, BAD is centered around 117.0°.[34] The plot of the static structure factor $S(Q)$ for 2-D and 3-D a-graphene shows a striking similarity between these structures. We obtain similar structures with a melt-quench approach with the *ab initio* code VASP (Fig. 1 and Table S1, ESI†).

In Fig. 3, the ring distribution shows that both 2-D and 3-D a-graphene have ring structures of various sizes (mostly 5, 6 and 7), as in shungite.[35] In contrast, both schwarzite and p-graphene exhibit 6-membered rings (exception: schwarzite has few 7-membered rings). We have also computed extended X-ray absorption fine structure (EXAFS) for our four models (see Fig. 4). EXAFS is valuable for the first-shell information.[36] We observe strong structural correlation of 3-D graphene and 2-D graphene in our EXAFS plot,[37,38] whereas pristine graphene and schwarzite structures distinctively differ from these structures. We show EXAFS signatures differentiating 2-D and 3-D a-G (a peak at ∼2.2 Å, see Fig. 4).

The electronic density of states (EDOS) and vibrational density of states (VDOS) are reported next. The low energy modes are related to the mechanical properties and low temperature thermal conductivity of a material.[39–42] The force constant matrix was obtained from a finite difference method displacing every atom in 6-directions ($\pm x$, $\pm y$, $\pm z$) with a small displacement of 0.015 cm^{-1}. The first three frequencies arising due to supercell translations which are very close to zero are neglected in our calculation and all our other frequencies are positive (no imaginary modes). Once again due to the gigantic size of our model, we have employed the Harris functional to our advantage with a double-ζ basis (see details[31,43]). Our 3-D amorphous graphene shows two distinctive components in VDOS (Fig. 5 (left panel)). A sharp peak around ∼814 cm^{-1}

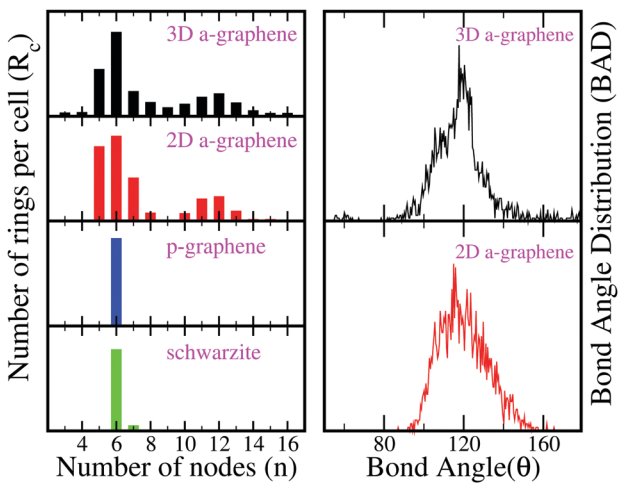

Fig. 3 Comparison of ring distribution between the four models and the plot of bond-angle distribution of 3-D and 2-D a-graphene.

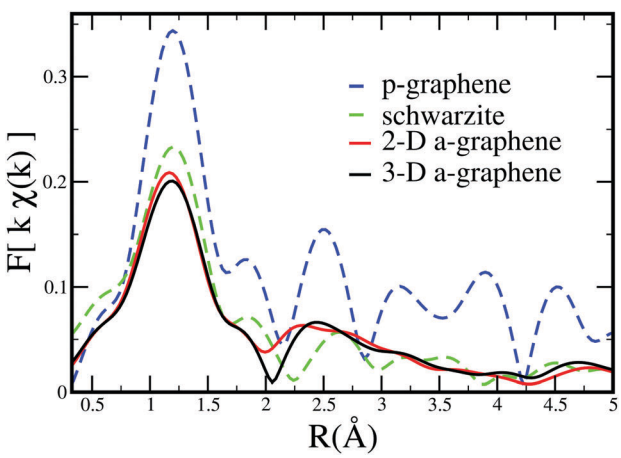

Fig. 4 Fourier transform of carbon K-edge EXAFS spectra [$k\chi(k)$] for the four models.

This journal is © the Owner Societies 2018

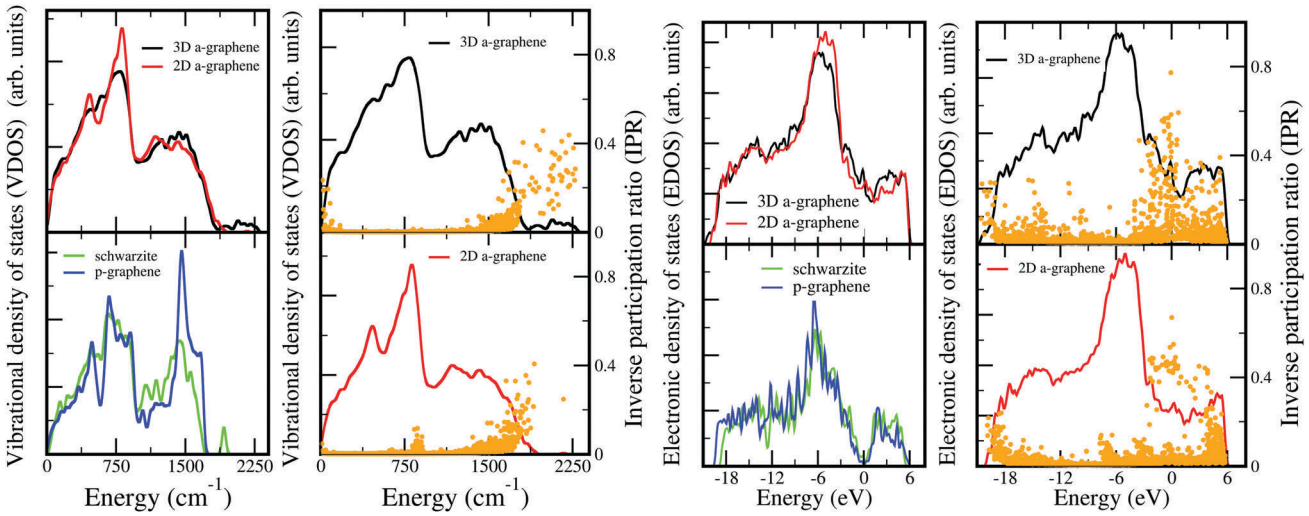

Fig. 5 (Left panel) Plot and comparison of the vibrational density of states for the four models. The 3-D graphene (a-carbon) has excellent similarity to the 2-D a-graphene. Yellow dots represent vibrational inverse participation ratio (IPR, eqn (1)). (Right panel) Plot and comparison of EDOS (E_F = 0 eV) and localization (IPR, yellow dots, eqn (2)).

and a broader peak at ~1300 cm^{-1}, and a narrow neck is observed at ~470 cm^{-1}. We have a surprising match of VDOS for our model and 2-D amorphous graphene. The VDOS for crystalline graphene and schwarzite reveal a different profile to amorphous graphene. The pristine graphene VDOS peaks are observed at: ~490 cm^{-1}, ~678 cm^{-1} and ~1460 cm^{-1}, with peak intensities and position quite different to amorphous graphene. We associate the peak at ~814 cm^{-1} with a-graphene and a peak around ~1460 cm^{-1} for p-graphene as signature peaks.

In Fig. 5 (right panel), we report the EDOS for these four models. The EDOS for both 3-D and 2-D graphene exhibit a striking similarity, and various defects (sp^3 and sp) and topology seem to have a modest effect. A similar observation was also seen in a ZrC-CDC structure.[14] Separate computations (not shown here) are in agreement with the previously established result of Van Tuan *et al.*[44] which showed that these materials are non conducting. We note that the EDOS of crystalline graphene and schwarzite are quite distinct from that of their amorphous counterpart. We define the inverse participation ratios for vibrations and electrons as:

$$\mathscr{I} = \frac{\sum_{i=1}^{N} \left|u_i^j\right|^4}{\left(\sum_{i=1}^{N} \left|u_i^j\right|^2\right)^2} \quad (1)$$

$$\mathscr{I}(\psi_n) = \frac{\sum a_i^4}{(\sum {a_i}^2)^2} \quad (2)$$

where, (u_i^j) is the normalized eigenvector of the jth mode and a_i are the components of the eigenvector projected onto atomic s, p, and d states.

The electronic and vibrational states of amorphous solids are affected by disorder present in the structure. The localization of electronic/vibrational states can be quantified by computing the inverse participation ratio (IPR).[45] A completely localized state would have an IPR value of unity while an extended state has a value of $(1/N)$, *i.e.* distributed over N atoms. Vibrational IPR is evaluated using the obtained normalized displacement vectors (u_i^j) as shown in eqn (1).[46] Similarly, the localization of the nth electronic state is computed as shown in eqn (2), where a_i is the component of the eigenvector projected onto the atomic s, p and d states (obtained from VASP).[45,47] By comparison of the localization of states for both 2D and 3D a-graphene near the Fermi energy, we see mostly extended states with few weakly localized states. We again obtain vibrational modes that are mostly extended, with a few localized modes around ~1800–2000 cm^{-1}. We further dissect the VDOS and EDOS into sp, sp^2 and sp^3 contributions to gain further insight into the 3D a-graphene model (Fig. 6). The decomposed VDOS shows that sp^2 bonding clearly dominates the vibrational spectrum.

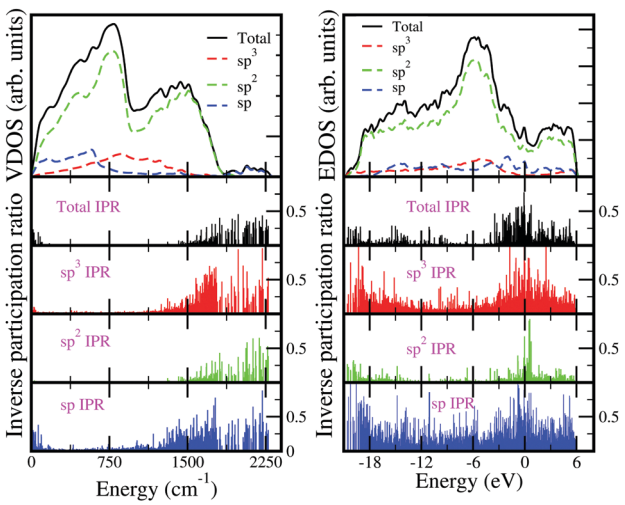

Fig. 6 (Left panel) Plot of total, (sp^3, sp^2, sp) projected VDOS and vibrational IPR for the 3-D a-graphene model. (Right panel) Plot showing total, (sp^3, $sp^2$and sp) projected EDOS and electronic IPR for the 3-D a-graphene model.

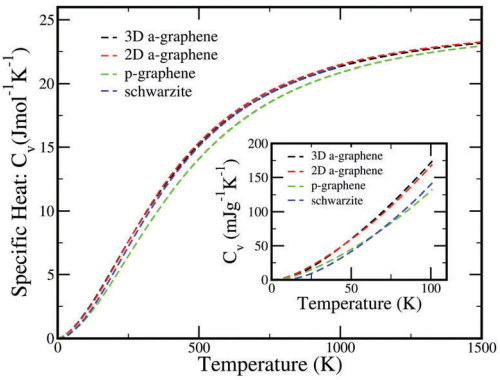

Fig. 7 Specific heat plots for the four models. (inset) Low temperature specific heat of the four models.

Furthermore, we can clearly observe the narrow neck at $\sim$470 cm^{-1}, seen in 2D a-G. We further decompose the vibrational localization into sp, sp^2 and sp^3 components. Most localization in this system is contributed by the sp and sp^3 bonds. Decomposition of EDOS into sp, sp^2 and sp^3 contributions shows quite an interesting result. The sp and sp^3 bonding atoms have almost no effect on the electronic properties both at the conduction band and deep into the valance band. Similar to VDOS, most of the electronic localization is due to sp and sp^3 bonded carbon networks. We have computed specific heat in the harmonic approximation, and $C_v(T)$ for the four models shows a similar pattern at high temperatures, with p-graphene showing slight deviation compared to the other models (see Fig. 7). The inset shows more prominent changes at the lower temperatures (0 K to 100 K). The two amorphous graphene models (2-D and 3-D) increase with the same slope between 0 K and 100 K. Meanwhile, a deviation from a-graphene is seen for the case of p-graphene and schwarzite.

4 Conclusions

In summary, we have shown that a-C with a density of 0.95 g cm^{-3} is a form of a-G. We provide a detailed analysis of our model by computing structural, vibrational and electronic properties and comparing to 2D amorphous graphene along with other sp^2 structures. Surprisingly, bonding defects ($\sim$11% sp^3 and $\sim$11% sp) have little effect on the properties like EDOS and VDOS.

Conflicts of interest

There are no conflicts to declare.

Acknowledgements

We thank Prof. Michael Treacy and Dr Ronald Cappelletti for helpful conversations. We thank the Ohio Supercomputer Center and NVIDIA Corporation for supercomputer time and a Tesla K40 GPU donation, respectively. We acknowledge US NSF grant under numbers: DMR 1506836, 1507118, 1507670 and 1507166. DAD thanks Prof. S. R. Elliott and Trinity College for hospitality.

Notes and references

1 J. Kotakoski, A. V. Krasheninnikov, U. Kaiser and J. C. Meyer, *Phys. Rev. Lett.*, 2011, **106**, 105505.
2 V. Kapko, D. A. Drabold and M. F. Thorpe, *Phys. Status Solidi B*, 2010, **247**, 1197–1200.
3 Y. Li, F. Inam, A. Kumar, M. F. Thorpe and D. A. Drabold, *Phys. Status Solidi B*, 2011, **248**, 2082–2086.
4 Y. Li and D. A. Drabold, *Phys. Status Solidi B*, 2013, **250**, 1012–1019.
5 H. Terrones, M. Terrones, E. Hernández, N. Grobert, J.-C. Charlier and P. M. Ajayan, *Phys. Rev. Lett.*, 2000, **84**, 1716–1719.
6 G. T. Barkema and N. Mousseau, *Phys. Rev. Lett.*, 1996, **77**, 4358–4361.
7 C. Z. Wang and K. M. Ho, *Phys. Rev. Lett.*, 1993, **71**, 1184–1187.
8 A. S. Sinitsa, I. V. Lebedeva, A. M. Popov and A. A. Knizhnik, *J. Phys. Chem. C*, 2017, **121**, 13396–13404.
9 B. Meredig and C. Wolverton, *Nat. Mater.*, 2012, **12**, 123.
10 P. Biswas, R. Atta-Fynn and D. A. Drabold, *Phys. Rev. B: Condens. Matter Mater. Phys.*, 2007, **76**, 125210.
11 G. Opletal, T. Petersen, B. Omalley, I. Snook, D. G. Mcculloch, N. A. Marks and I. Yarovsky, *Mol. Simul.*, 2002, **28**, 927–938.
12 A. K. Soper, *Mol. Phys.*, 2001, **99**, 1503–1516.
13 A. H. Farmahini and S. K. Bhatia, *Carbon*, 2015, **83**, 53–70.
14 M. J. Lopez, I. Cabria and J. A. Alonso, *J. Chem. Phys.*, 2011, **135**, 104706.
15 Computer simulation of the structure of nanoporous carbons and higher density phases of carbon in Many-body Approaches at Different Scales, a tribute to Norman H. March, Springer, p. 21.
16 C. de Tomas, I. Suarez-Martinez, F. Vallejos-Burgos, M. J. Lopez, K. Kaneko and N. A. Marks, *Carbon*, 2017, **119**, 1–9.
17 A. Pandey, P. Biswas and D. A. Drabold, *Sci. Rep.*, 2016, **6**, 33731.
18 A. Pandey, P. Biswas and D. A. Drabold, *Phys. Rev. B: Condens. Matter Mater. Phys.*, 2015, **92**, 155205.
19 A. Pandey, P. Biswas, B. Bhattarai and D. A. Drabold, *Phys. Rev. B: Condens. Matter Mater. Phys.*, 2016, **94**, 235208.
20 B. Bhattarai, A. Pandey and D. Drabold, *Carbon*, 2018, **131**, 168–174.
21 D. Igram, B. Bhattarai, P. Biswas and D. Drabold, *J. Non-Cryst. Solids*, 2018, **492**, 27–32.
22 H. Terrones and M. Terrones, *New J. Phys.*, 2003, **5**, 126.
23 A. H. Farmahini, G. Opletal and S. K. Bhatia, *J. Phys. Chem. C*, 2013, **117**, 14081–14094.
24 M. G. Tucker, D. A. Keen, M. T. Dove, A. L. Goodwin and Q. Hui, *J. Phys.: Condens. Matter*, 2007, **19**, 335218.
25 J. M. Soler, E. Artacho, J. D. Gale, A. Garcia, J. Junquera, P. Ordejon and D. Sanchez-Portal, *J. Phys.: Condens. Matter*, 2002, **14**, 2745–2779.
26 G. Kresse and D. Joubert, *Phys. Rev. B: Condens. Matter Mater. Phys.*, 1999, **59**, 1758–1775.
27 G. Kresse and J. Furthmuller, *Phys. Rev. B: Condens. Matter Mater. Phys.*, 1996, **54**, 11169–11186.

This journal is © the Owner Societies 2018

28 P. E. Blochl, *Phys. Rev. B: Condens. Matter Mater. Phys.*, 1994, **50**, 17953–17979.
29 M. Hacene, A. Anciaux-Sedrakian, X. Rozanska, D. Klahr, T. Guignon and P. Fleurat-Lessard, *J. Comput. Chem.*, 2012, **33**, 2581–2589.
30 M. Hutchinson and M. Widom, *Comput. Phys. Commun.*, 2012, **183**, 1422–1426.
31 B. Bhattarai and D. A. Drabold, *Carbon*, 2017, **115**, 532–538.
32 V. L. Deringer, N. Bernstein, A. P. Bartók, M. J. Cliffe, R. N. Kerber, L. E. Marbella, C. P. Grey, S. R. Elliott and G. Csányi, *J. Phys. Lett.*, 2018, **9**, 2879–2885.
33 R. Atta-Fynn and P. Biswas, *J. Chem. Phys.*, 2018, **148**, 204503.
34 D. Beeman, J. Silverman, R. Lynds and M. R. Anderson, *Phys. Rev. B: Condens. Matter Mater. Phys.*, 1984, **30**, 870–875.
35 G. Zhao, P. Buseck, A. Rougée and M. Treacy, *Ultramicroscopy*, 2009, **109**, 177–188.
36 A. Filipponi, F. Evangelisti, M. Benfatto, S. Mobilio and C. R. Natoli, *Phys. Rev. B: Condens. Matter Mater. Phys.*, 1989, **40**, 9636–9643.
37 J. J. Rehr, J. J. Kas, F. D. Vila, M. P. Prange and K. Jorissen, *Phys. Chem. Chem. Phys.*, 2010, **12**, 5503–5513.
38 M. Newville, *J. Synchrotron Radiat.*, 2001, **8**, 322–324.
39 S. Berber, Y.-K. Kwon and D. Tománek, *Phys. Rev. Lett.*, 2000, **84**, 4613–4616.
40 J. Hone, B. Batlogg, Z. Benes, A. T. Johnson and J. E. Fischer, *Science*, 2000, **289**, 1730–1733.
41 A. A. Balandin, *Nat. Mater.*, 2011, **10**, 569.
42 T. Zhu and E. Ertekin, *Nano Lett.*, 2016, **16**, 4763–4772.
43 B. Bhattarai and D. A. Drabold, *J. Non-Cryst. Solids*, 2016, **439**, 6–14.
44 D. Van Tuan, A. Kumar, S. Roche, F. Ortmann, M. F. Thorpe and P. Ordejon, *Phys. Rev. B: Condens. Matter Mater. Phys.*, 2012, **86**, 121408.
45 J. M. Ziman, *Models of disorder*, Cambridge University Press, 1979.
46 S. N. Taraskin and S. R. Elliott, *Phys. Rev. B: Condens. Matter Mater. Phys.*, 1997, **56**, 8605–8622.
47 C. Chen and J. Robertson, *J. Non-Cryst. Solids*, 1998, **227–230**, 602–606.